X-RAY IMAGING OF SUPERCONDUCTING RF CAVITIES[*]

S. Musser,[†] J. Bierwagen, T. Grimm, W. Hartung

National Superconducting Cyclotron Lab, Michigan State University, East Lansing, Michigan

Abstract

The goal of this research is to develop an improved diagnostic technique to locate field emission sources in superconducting radio frequency cavities. The present technique can be used after the cavities are installed in an accelerator, unlike existing techniques such as temperature mapping. Field emitted electrons are accelerated by the RF field and strike the cavity walls, producing Bremsstrahlung x-rays. The locations of the x-ray sources can be determined using a collimated sodium iodide detector moving along the cavity outside the cryostat. The sodium iodide detector measures the energy spectrum of the x-rays, with the maximum x-ray energy being equal to the kinetic energy of the impacting electrons. A particle tracking code is used to infer the locations of the electron emitters and the emitter parameters. X-ray imaging measurements were done on a prototype cryomodule containing two 6-cell 805 MHz $\beta = 0.47$ cavities. The results and analysis of cavity #2 will be presented. Measurements were done on several modes in the TM_{010} pass-band, in addition to the accelerating mode ($TM_{010}\pi$). The electron trajectories and electron impact locations are different for different pass-band modes, providing a method to check the consistency of the emitter locations and parameters inferred from the simulations.

INTRODUCTION

Field emission (FE) in superconducting radio frequency (SRF) cavities is a common problem which causes degradation in the high-field performance. Sources of field emission include surface roughness, dust or micro-particles, grain boundaries, adsorbed gas, and impurities in the metal itself.

FE is normally a steady state phenomenon, but RF breakdown can occur when regular FE currents increase exponentially as the electric field is increased. RF breakdown limits the operation of accelerators and can cause irreversible damage to their physical structures. The sequence of events leading to RF breakdown varies, but typically, when under high gradient operation, x-rays and temperature changes appear before a structure begins to break down.

The field-emitted electrons are accelerated by the RF field and strike the cavity wall, generating Bremsstrahlung x-rays. These x-rays have been detected on general radiation monitoring systems and coincide with a decrease of the quality factor (Q) value while the electric field is increased [1]. Although x-ray monitoring is a useful diagnostic, the locations of the x-ray sources and corresponding electron emitters cannot be identified.

X-ray images of a single-cell cavity have been taken through a Dewar and magnetic shield using a lead "pin-hole camera" and high sensitivity re-useable x-ray film [2]; this approach has proven successful but lacks energy information.

Carbon resistors placed on the cavity wall have been used for thermometric diagnostics of cavities to identify the actual electron impact location(s). Particle tracking codes were then used to locate the source of the field-emitted electrons [1, 3]. This system has also proven successful, and has been used by several labs, but is not suitable for operating accelerators.

We were able to pinpoint the regions of x-ray emission (intensity and energy spectrum) by using a collimated sodium iodide (NaI) detector placed outside the cryostat. The electric field has a different amplitude and direction for each cell and for each mode of excitation. For different modes of excitation one can expect different electron trajectories and impact locations for the same emitter locations. Measurements were done on the π, $5\pi/6$, and $4\pi/6$ modes in the TM_{010} pass-band, thus providing a method to check the consistency of the emitter locations and parameters inferred from simulations.

The x-ray imaging accurately locates the source(s) and energies of x-rays. Knowing the location of the x-rays and the maximum electron kinetic energy, a particle tracking simulation was used to determine the location of the source of electrons and thus of surface defects. Preliminary work in x-ray imaging of cavities was presented in an earlier paper [4].

X-ray imaging makes it possible to identify defects in operating accelerators; we hope that this technique can become a useful diagnostic tool for SRF research and development.

DESIGN

The data for this study were collected at the National Superconducting Cyclotron Laboratory at Michigan State University during a horizontal test of two $\beta = 0.47$ 6-cell cavities at 805 MHz developed for the Rare Isotope Accelerator (RIA) [5, 6, 7].

A detector with slit collimation, moving perpendicular to the slit orientation along the entire cavity length, was used to locate the source of x-rays in one plane (Figure 1). The front of the detector assembly was placed 40 mm from the outer cryostat wall. A 1.8 mm slit collimator through 102 mm of lead provided a full width half maximum horizontal resolution of 6.8 to 8.4 mm.
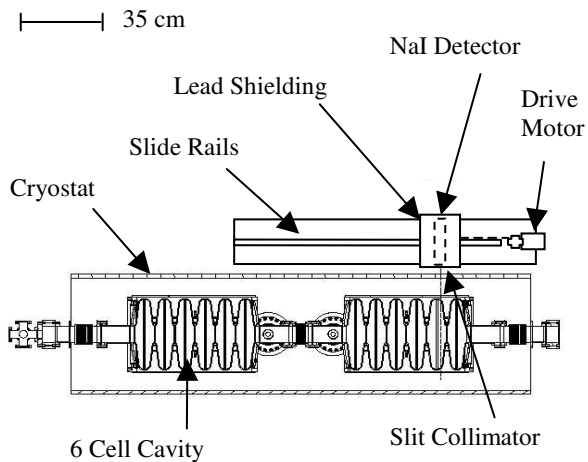
Figure 1. Top view of slit collimator scanning the cryostat in the horizontal direction.

Detector

The x-ray spectrum was measured with an ORTEC 50 mm by 50 mm integral NaI crystal and photomultiplier tube. Sodium iodide was chosen as the scintillator since it provides adequate energy resolution and good efficiency.

Data Acquisition

Data were acquired with an ORTEC digiDART portable multi-channel analyzer (MCA), interfaced to a local computer through the universal serial bus (USB) port, and controlled through a LABVIEW 7.0 program. Data were collected at two-second intervals. Two scans of the cryostat were made for each mode of excitation, to ensure that the data were reproducible.

Data Analysis

The regions of x-ray emission (intensity and energy spectrum) for each 6-cell $\beta = 0.47$ cavity were located from outside the cryostat. Compton scattering was the predominant x-ray interaction for the range of energies measured and cryostat materials used. When an x-ray is Compton scattered, only a fraction of its energy is imparted to an electron. The x-ray continues traveling at a lower energy, on a different trajectory, and experiencing additional interactions. The electron travels a short distance, losing energy in ionizing and radiative collisions. Therefore, Compton scattering increases the intensity of x-rays in low energy channels, while reducing the count rate in high-energy channels. The energy spectrum of the x-rays reaches zero at the energy of the impacting field emission electrons generating the x-rays. This energy is compared to the impact energy predicted by the particle tracking code.

The detector assembly was placed in a lead housing so only x-rays traveling through the collimator would enter the detector. A 3.4 mm thick lead filter was placed in front of the collimator. This attenuated nearly 100% of the x-rays below 0.2 MeV and 65% at 0.5 MeV.

With the slit collimator closed, a horizontal scan was made and data were accumulated with the cavity at the

same field level. This background signal was subtracted from the data.

Field Emission Simulation

For the π mode of excitation, an electron tracking code was used to trace the source of electrons, producing the Bremsstrahlung x-rays, to their point of origin. The software not only predicts the trajectories of field-emitted electrons, but also their impact sites, impact energies, and the resulting power deposition along the inner surface of the cavity. The electron tracking code has been used in the past for field emission [3] and multipacting [8] simulations. The electromagnetic field for the tracking code is calculated using SuperLANS [9].

EXPERIMENTAL RESULTS

During horizontal testing of the two 6-cell cavities, data were accumulated for the π, $5\pi/6$, and $4\pi/6$ modes of excitation in the TM_{010} passband.
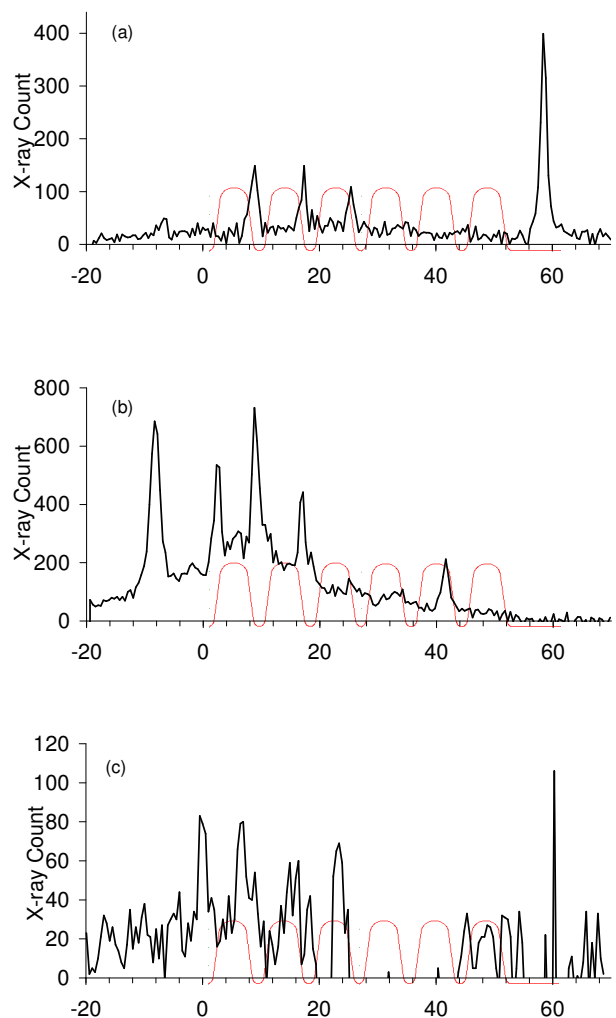

Figure 2. Total flux of x-rays for a horizontal scan in the (a) π, (b) $5\pi/6$, and (c) $4\pi/6$ modes of excitation in the TM_{010} pass-band. The field levels are $E_p = 22$ MV/m, $E_p \approx 25.5$ MV/m, and $E_p \approx 24.9$ MV/m, respectively. The horizontal axis is the distance along the cavity in cm.

X-Ray Scans

The total number of x-rays entering the detector along the length of cavity #2 is shown in Figure 2. The horizontal axis is the detector travel distance in cm and the vertical axis is the total number of x-rays entering the detector (the cavity silhouette is superimposed on the data). Note that the vertical scales are different for each mode. Data were examined above a 0.4 MeV threshold in order to distinguish an actual x-ray source from Compton scattered x-rays. The background count of x-rays was subtracted from the data. Each data point was two seconds of accumulation, which corresponds to an axial scan distance of 0.45 cm, due to the continuous motion of the detector. For the π mode, the stored energy was obtained from RF measurements, and the peak surface electric field (E_p) was inferred from the stored energy. For the $5\pi/6$ and $4\pi/6$ modes, an estimate for E_p was obtained from the pick-up antenna signal relative to that of the π mode, taking into account the field distributions predicted by SuperLANS.

The x-ray energy spectrum for the high intensity peak at 78.5 cm in Figure 2a is shown in Figure 3. X-ray energies for the five peaks of the π mode (Figure 2a) ranged from 0.72 to 1.2 MeV, from 0.94 to 1.2 MeV for the five peaks of the $5\pi/6$ mode (Figure 2b), and from 0.84 to 0.94 MeV for the four peaks of $4\pi/6$ mode (Figure 2c).

Graphing analysis software to better determine the end-point energy of the spectra including error, are being considered.

RF Measurements

The electric field was held nearly constant during the x-ray imaging. The quality factor (Q) was calculated from the RF measurements. Previous tests, when the electric field was varied, showed a low-field Q of about 10^{10}, as can be seen in Figure 4. High power pulsed processing is responsible for the increase in Q and the higher E_p for the second test. Some x-ray imaging measurements were done at higher temperatures ($T = 2.1$ K) where the low-field Q was smaller, but emission should be insensitive to temperature. The Q during x-ray imaging matches most closely with the RF measurements of 7 May 2004.
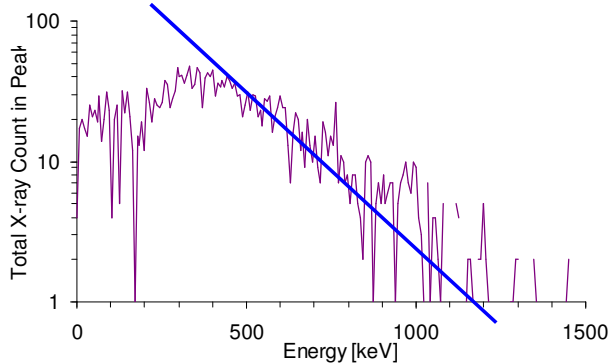
Figure 3. A π mode x-ray energy spectrum of high intensity peak at 78.5 cm of Figure 2a. Endpoint energy, i.e. electron energy, is near 1200 keV.
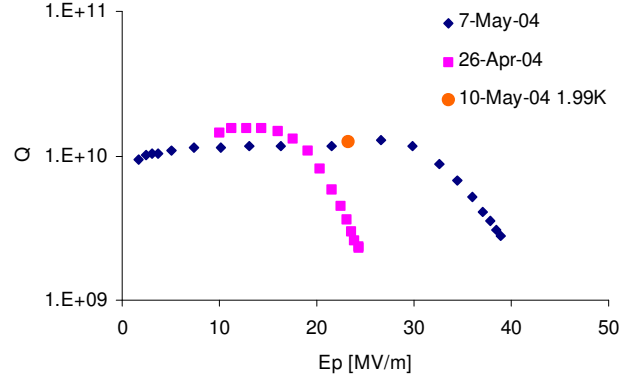
Figure 4. Quality factor versus peak electric field for two tests on cavity #2 where the electric field was varied. The Q during x-ray imaging is about 10^{10} at 2 K (orange circle), which matches the RF measurements of 7 May 2004 (diamonds).

The average cavity current I should depend on the Fowler-Nordheim (FN) field enhancement factor β_{FN} [1]:

$$I \propto (\beta_{FN}E)^{2.5} \exp\left(\frac{-B_{FN}\phi^{\frac{3}{2}}}{\beta_{FN}E}\right),\qquad(1)$$

where E is the electric field at the emitter, B_{FN} is a constant, and ϕ is the work function of the metal. Published values of ϕ for niobium range from 4.0 to 4.9 eV, depending on the crystal orientation [10]; we assumed $\phi = 4.3$ eV. The numerical value of B_{FN} depends on what approximations are made. We used the value of Loew and Wang [11], which gives $B_{FN}\phi^{3/2} = 5.82 \times 10^{10}$ V/m.

We were not able to measure the current directly, but we inferred the total power dissipation (P_d) as a function of field level from RF measurements. We also measured the x-ray signal from an ion chamber as a function of field level. The ohmic power dissipation (P_0) was calculated from the low-field Q. To obtain the power dissipated due purely to field emission, we subtracted P_0 from P_d. Since the power
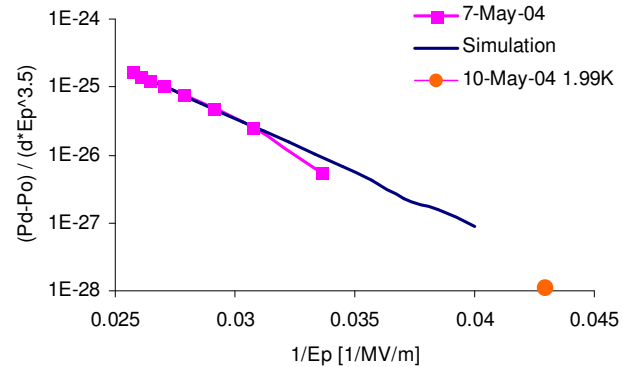
Figure 5. Fowler-Nordheim plot of the RF measurements. The slope of the data (pink squares) corresponds to a β_{FN} value between 100 and 180. The data can be reproduced well by particle tracking simulations (blue line) with $\beta_{FN} \approx$ 150. The orange circle is a data point taken during x-ray imaging.
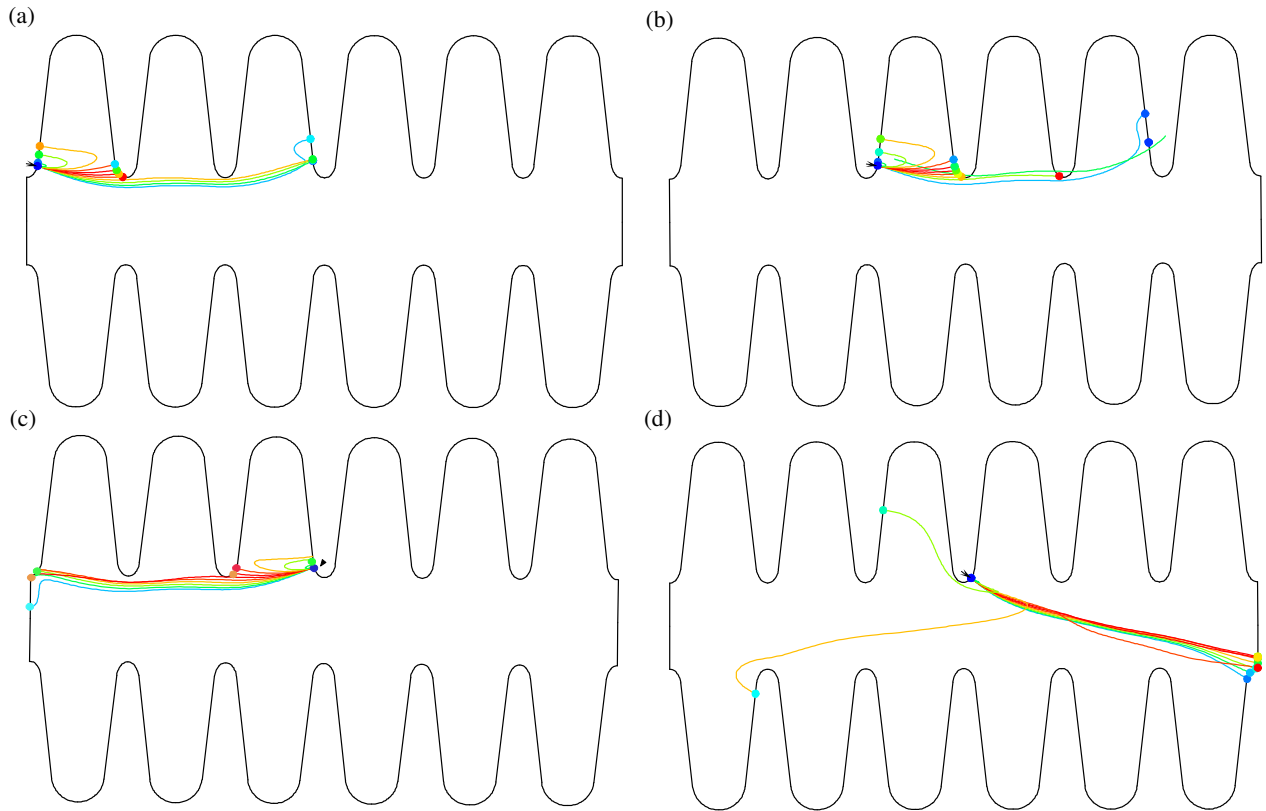
(a)

(b)

(c)

(d)

Figure 6. Emission sites and corresponding electron trajectories for the π mode with an emitter in (a) the first, (b,c) the third, and (d) the fourth cell of the cavity. The black arrows indicate the emitter locations. The trajectories are color-coded according to the time of emission, with blue for emission at the lowest electric field and red for emission at the highest electric field. The impact sites are color coded dots indicating electron final kinetic energy, where blue is a minimum and red a maximum. The E_p value is 22 MV/m for all four cases.

is the product of the voltage and the current, an additional factor of $E_p d$ was assumed when reformulating Equation (1) in terms of field emission power; d is the effective distance over which the field emission electrons are accelerated with an electric field equal to E_p. For present purposes, we assumed $d = 1$ m. A semi-log plot of the power divided by $E_p^{3.5} d$ should be a straight line (Figure 5). The electric field at the emitter is not known, so we assume $E \approx E_p$ to calculate β_{FN}. The slope of the line for the RF data after pulsed processing is consistent with a value of β_{FN} between 100 and 180 (Figure 5). We obtained $\beta_{FN} \approx 340$ for the RF measurements before pulsed processing (not shown in Figure 5).

The x-ray signal from the ion chamber should be proportional to the field emission power. A β_{FN} value was obtained from the x-ray measurements to cross-check the RF measurements. The β_{FN} value was within 25% of that obtained from the RF data.

SIMULATION RESULTS

We attempted to reproduce the x-ray distributions and x-ray energies of the π mode scan of Figure 2a with the simulations. Four emitters were sufficient to reproduce the measured distribution of x-ray intensities and energies in the simulations. Emitter sites, trajectories, and impact sites

Table 1. Emitter locations and parameters obtained from the simulations. S is the distance along the cavity surface measured from the cell equator; A_E is the effective emitter area.

Cell Number	S (cm)	β_{FN}	A_E (cm^2)	E/E_p
1	-13.0	150	9.13×10^{-12}	0.94
3	-12.9	155	8.05×10^{-12}	0.92
3	$+13.1$	145	1.49×10^{-11}	0.95
4	-13.7	140	1.63×10^{-11}	0.95

are shown in Figure 6. The emitter locations are listed in Table 1. A β_{FN} of 100 was used for the simulations, based on the slope from the RF data. For the emitter locations given in Table 1, the local field values range from $0.92E_p$ to $0.95E_p$.

The particle tracking simulation can be used to calculate the power dissipation without the simplifying assumptions used above to obtain β_{FN} from the slope of the RF data. By choosing β_{FN} and emitter areas for each of the proposed emission sites, the consistency of the RF measurements can be checked. As can be seen in Figure 5, the power dissipation predicted by the simulations can be made to agree well with the measured values. The corresponding emitter parameters are included in Table 1. The β_{FN} values are about

150, consistent with the values obtained from the slope of the RF data, and emitter areas are of order 10^{-11} cm^2. The areas and field enhancement factors are within the range of previously measured values [1]. Higher β_{FN} values (150 instead of 100, as originally assumed) could produce some change in the intensity distributions. This must still be checked.

A single emitter is sufficient for consistency with the RF data, but four emitters are needed to explain the peaks in the x-ray imaging scan (Figure 2a). For a given set of β_{FN} values, the RF data can be used to determine the sum of emitter areas, but they do not contain enough information to fix the relative proportions. The area values in Table 1 assume equal power contributions from each of the emitters. The relative intensities of the x-ray peaks do constrain the emitter areas relative to each other, however. This analysis is still in progress.

Other emitter locations can also account for the observed peaks, so the additional measurements in the other passband modes will be used to check the consistency of emitter locations. A plot of the surface electric field for each mode is shown in Figure 7, along with emitter locations found for the π mode. The π mode emitters were found in regions of high surface electric field which, in general, coincide with high surface electric field regions for the $5\pi/6$ and $4\pi/6$ modes. One counter example is the left-most emitter, for which the surface field is low in the case of the $4\pi/6$ mode.

Work is presently underway to simulate the electron trajectories for other passband modes. Periodic boundary conditions are being considered for this purpose. Electron emission sites for the $5\pi/6$ and $4\pi/6$ modes should be consistent with the emission sites found for the π mode.

CONCLUSION

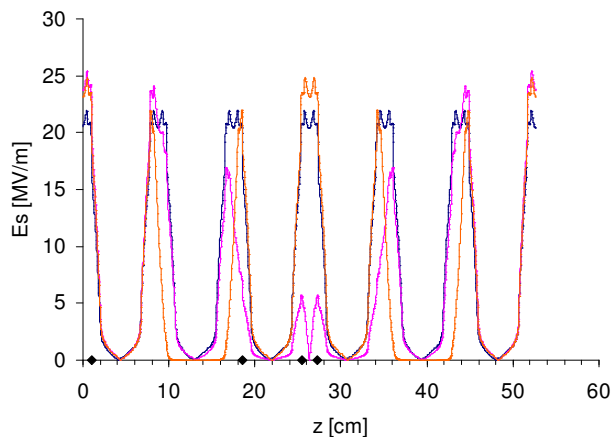We have shown that x-ray imaging can locate x-ray sources inside a cryostat for multiple passband modes in a multi-cell SRF cavity. Simulation codes track the field emitted electrons and allow us to infer the emitter locations. By taking spectra for different modes of excitation, the emitter locations can be checked. It is hoped that x-ray imaging can be used to locate x-ray sources in operating accelerators.

REFERENCES

[1] H. Padamsee *et al.*, *RF Superconductivity for Accelerators*, John Wiley & Sons, Inc., 1998.

[2] T. L. Grimm *et al.*, in *Proceedings of the Tenth Workshop on RF Superconductivity: Tsukuba, Japan, 2001*, p. 86–90.

[3] H. Padamsee *et al.*, in *Proceedings of the 1987 IEEE Particle Accelerator Conference*, p. 1824–1826.

[4] S. E. Musser *et al.*, in *Proceedings of the 2003 Particle Accelerator Conference*, p. 1356–1358.

[5] C. C. Compton *et al.*, *Phys. Rev. ST Accel. Beams* **8**, 042003 (2005).

[6] T. L. Grimm *et al.*, in *Proceedings of the 2003 Particle Accelerator Conference*, p. 1350–1352.

[7] T. L. Grimm *et al.*, in *Proceedings of the XXII International Linear Accelerator Conference: Lübeck, Germany, 2004*, p. 773–775.

[8] W. Hartung *et al.*, in *Proceedings of the Tenth Workshop on RF Superconductivity: Tsukuba, Japan, 2001*, p. 627–631.

[9] D. G. Myakishev and V. P. Yakovlev, in *Proceedings of the 1991 Particle Accelerator Conference*, p. 3002–3004.

[10] David R. Lide, Editor, *CRC Handbook of Chemistry and Physics*, 83rd Edition, CRC Press, Boca Raton, 2002.

[11] Gregory A. Loew & J. W. Wang, Report SLAC-PUB-4647, SLAC, Stanford, California (1988).

Figure 7. Surface electric field for the π mode (blue), $5\pi/6$ mode (pink), and $4\pi/6$ mode (red). The E_p values are the same as for Figure 2. The emitter locations hypothesized for the π mode are also shown (diamonds). The fields were calculated with SuperLANS.